



Platinum partitioning between metal and silicate melts: Core formation, late veneer and the nanonuggets issue

Etienne Médard, Max W. Schmidt, Markus Wälle, Nicole Keller, Detlef
Günther

► To cite this version:

Etienne Médard, Max W. Schmidt, Markus Wälle, Nicole Keller, Detlef Günther. Platinum partitioning between metal and silicate melts: Core formation, late veneer and the nanonuggets issue. *Geochimica et Cosmochimica Acta*, 2015, 162, pp.183-201. 10.1016/j.gca.2015.04.019 . hal-01172449

HAL Id: hal-01172449

<https://hal.science/hal-01172449>

Submitted on 2 Feb 2021

HAL is a multi-disciplinary open access archive for the deposit and dissemination of scientific research documents, whether they are published or not. The documents may come from teaching and research institutions in France or abroad, or from public or private research centers.

L'archive ouverte pluridisciplinaire **HAL**, est destinée au dépôt et à la diffusion de documents scientifiques de niveau recherche, publiés ou non, émanant des établissements d'enseignement et de recherche français ou étrangers, des laboratoires publics ou privés.

Platinum partitioning between metal and silicate melts: core formation, late veneer and the nanonuggets issue.

Etienne Médard^{1,2*}, Max W Schmidt², Markus Wälle^{2,3}, Nicole S Keller^{4,5}, Detlef Günther³

¹ *Laboratoire Magmas et Volcans, Université Blaise Pascal - CNRS - IRD, OPGC, 5 rue Kessler, 63038 Clermont Ferrand, France*

² *Institut für Geochemie und Petrologie, ETH Zürich, Clausiusstrasse 25, CH-8092 Zürich, Switzerland*

³ *Laboratory of Inorganic Chemistry, ETH Zürich, Wolfgang-Pauli-Strasse 10, CH-8093 Zürich, Switzerland*

⁴ *University of Iceland, Institute of Earth Sciences, Sturlugata 7, IS-101 Reykjavik, Iceland*

⁵ *Research School of Earth Sciences, Australian National University, Canberra, ACT 0200, Australia*

***Corresponding author:**

Etienne Médard
Laboratoire Magmas et Volcans
Université Blaise Pascal – CNRS – IRD, OPGC
5 rue Kessler
F-63038 Clermont-Ferrand Cedex, France
E.Medard@opgc.univ-bpclermont.fr
Phone: +33 686 697 599

Abstract:

High-pressure, high-temperature experiments have been performed at ~1.2 GPa and 1360-2100 °C to investigate the partitioning of Pt between a silicate melt and a metallic melt. Our experiments indicate that nanonuggets encountered in previous experiments are experimental artifacts, formed at high temperature by oversaturation caused by high oxygen fugacity during the initial stages of an experiment. Experiments at high-acceleration using a centrifuging piston-cylinder show that nanonuggets can be removed by gravity during the experiment. Formation of nanonuggets can also be avoided by using initially reduced starting materials. The presence of iron is also a key element in reducing the formation of nanonuggets. Our nanonugget-free data are broadly consistent with previous nanonuggets-filtered data, and suggest that Pt partitioning becomes independent of oxygen fugacity below an oxygen fugacity of at least IW+2. Pt is thus possibly dissolved as a neutral species (or even an anionic species) at low fO_2 , instead of the more common Pt^{2+} species present at higher fO_2 . Due to low concentration, the nature of this species cannot be determined, but atomic Pt or Pt^- are possible options. Under core-formation conditions, Pt partitioning between metal and silicate is mostly independent of oxygen fugacity, silicate melt composition, and probably also pressure. Partition coefficient during core formation can be expressed by the following equation: $\log D_{Pt}^{M_{metal}/silicate} = 1.0348 + 14698/T$ (in weight units). Calculations indicate that the Pt content (and by extension the Highly Siderophile Elements content) of the Earth's mantle cannot be explained by equilibrium partitioning during core formation, requiring further addition of HSE to the mantle. The mass of this late veneer is approximately 0.4 % of the total mass of the Earth (or 0.6 % of the mass of the mantle).

1. Introduction: Highly Siderophile Elements and the nanonugget issue

Highly Siderophile Elements (hereafter referred to as HSE) are a class of transition metals that have a strong affinity for liquid or solid metallic alloys during geochemical processes. The HSE group is usually defined as the group of elements with metal/silicate partition coefficients greater than 10^4 at 1 bar, and includes Au, Re, and the platinum group elements (Ru, Rh, Pd, Os, Ir, Pt). Their geochemical affinity for metals makes the HSE excellent tracers for core formation processes in the terrestrial planets, since they are strongly partitioned into the core forming Fe-alloy. Some of the HSE are also involved in key radioisotope systems ($^{190}\text{Pt}/^{186}\text{Os}$, $^{187}\text{Re}/^{187}\text{Os}$, $^{107}\text{Pd}/^{107}\text{Ag}$, Carlson et al., 2008).

The most simple core formation models for the Earth involve equilibration between core-forming metal and mantle-forming silicate melts in a high-temperature magma ocean (see Ringwood, 1977, and a recent review in Righter, 2011). If core segregation was a simple equilibrium process, then the chemical composition of the mantle would record the last equilibration of the two melts at the base of the magma ocean. Since partition coefficients for various siderophile elements vary strongly as a function of temperature, oxygen fugacity, and for some of them possibly pressure (e.g., Ni and Co, Chabot et al., 2005), it would be possible to extract equilibrium conditions from the actual composition of the Earth's mantle combined with a reasonable assumption on bulk Earth composition. The mantle content of moderately siderophile elements can indeed be reproduced by high-temperature equilibration at lower mantle pressures (e.g., ~ 30 GPa and ~ 3300 K, Bouhifd and Jephcoat, 2011; Righter, 2011). A more complex class of core formation models involves heterogeneous accretion during which the oxygen fugacity and/or the composition of accreted material change (Rubie et al., 2011; Wade and Wood, 2005). Incomplete equilibration of the latest accreted material may add further complexity (Rubie et al., 2011). One important cornerstone of these models is the partitioning of the moderately siderophile elements; however, they can generally not account for the highly siderophile element concentrations of the Earth's mantle.

HSE concentrations in the Earth's mantle (~ 0.005 - 0.009 times CI-chondrites concentrations, Becker et al., 2006; Palme and O'Neill, 2003) are low, yet higher than predicted by equilibrium core formation processes. Nevertheless, for most HSE, partitioning data are scarce and most metal-silicate partition coefficients are derived from solubility experiments in iron-free systems which may or may not apply to the formation of an iron-rich core. For example, only three Pt partitioning studies using Fe- and Mg- bearing compositions

have been published so far (Bennett et al., 2014; Cottrell and Walker, 2006; Mann et al., 2012).

Secondly, most of the HSE show nearly chondritic element ratios in the mantle despite their diverse geochemical behavior (Becker et al., 2006; Lorand et al., 2008). These observations have led to a long-standing controversy between two schools of thought: (1) HSE concentrations in the mantle are the result of core formation processes, either under conditions not yet investigated experimentally or through complex, possibly non-equilibrium processes; (2) very low HSE concentrations in the mantle acquired through core formation processes are overprinted by the later addition of (oxidized) material that does not contribute to core formation (the “late veneer”, Chou, 1978).

However, despite experimental and analytical progress, the partitioning of HSE between silicate melts and metallic melts/alloys is still poorly known under the expected geological high-pressure, high-temperature conditions (Ertel et al., 2008) which include variable oxygen fugacity (from \leq IW-2 for core formation to \sim FMQ for upper mantle melting). In the case of Pt, probably the best studied HSE, the first studies at atmospheric pressure (Amossé and Allibert, 1993; Borisov and Palme, 1997; Ertel et al., 1999; Fortenfant et al., 2003) were limited to 1550 °C by the eutectic melting of the Pt-Fe alloy loops used for the experiments. High-pressure experiments (Ertel et al., 2006; Holzheid et al., 2000) expended the range of investigated conditions, but were limited in temperature by the use of Pt capsules and in oxygen fugacity by the presence of nanonuggets. HSE concentrations in experimental silicate glasses are indeed often characterized by a very poor reproducibility, in particular at low concentrations, i.e., at low oxygen fugacities and temperatures. Time-resolved analyses by LA-ICP-MS produce noisy signals characterized by spikes or broad hills and highly unstable count rates (Ertel et al., 2008; Keller, 2008; O'Neill et al., 1995). Those hills and spikes have been attributed to the presence of small metal particles or “nanonuggets”, with estimated sizes between 50 nm and 10 μ m (e.g., Cottrell and Walker, 2006; Ertel et al., 1999; Fortenfant et al., 2006; Simon et al., 2007). The origin of these nanonuggets has been a matter of heated debate and they have been variably interpreted as (1) quench phenomena (Cottrell and Walker, 2006; Simon et al., 2007), or (2) equilibrium particles resulting from physical processes during the experiment (Borisov and Palme, 1997; Ertel et al., 2008; Ertel et al., 2006; O'Neill et al., 1995). Whether these nanonuggets are considered to be present at run temperature (and thus excluded from the bulk concentration) or quench phases (and thus re-integrated into the bulk concentration) results in orders of magnitude of variation in partition coefficients for platinum group elements (Cottrell and Walker, 2006; Ertel et al., 2006).

Identifying the nature and the formation processes of nanonuggets is thus a key issue for high-quality HSE partitioning data.

In this paper, we investigate Pt partitioning between natural Fe-bearing silicate melt and metallic melt/alloy as a function of temperature and oxygen fugacity at pressures of 0.7 – 1.8 GPa, and temperatures between 1360 and 2100 °C. The main goals are to understand the nature of nanonuggets and the processes that lead to their formation, and to develop a model for Pt partitioning. As a by-product, we also developed new techniques to produce nanonugget-free HSE-bearing silicate glasses at high pressures and temperatures. The results are then used to estimate the need for a late-veneer during the last stage of Earth accretion.

2. Experimental and analytical techniques

2.1. Starting materials

All experiments have been performed in piston-cylinders using high-purity graphite capsules. Three basaltic starting materials with near-identical major element compositions were used (Table 1): (1) for most experiments, a natural high-alumina tholeiitic basalt (82-72f, Donnelly-Nolan et al., 1991), (2) an oxidized Pt-bearing glass made from the natural basalt, and (3) a synthetic Pt-free reduced glass. The oxidized Pt-rich glass was made by attaching powdered 82-72f basalt onto a Pt-wire loop using polyvinyl alcohol as a binder, and glassing it at 1350 °C in air for 48 hours. Under those conditions, ~70 mol% of the iron is expected to be present as Fe³⁺ (Kress and Carmichael, 1991), and the glass is enriched in Pt (3.2 ± 0.7 ppm Pt measured by LA-ICP-MS, Table 1). The reduced, Pt-free glass was made from a gel, burned at 800 °C in air for 48 hours in an alumina crucible, then reacted with pure metallic Fe in a graphite capsule at 1400 °C and 1.2 GPa for more than 48 hours in a piston-cylinder. At the end of the experiments, this silicate glass is in equilibrium with a Fe-C alloy containing 5.3 ± 0.2 wt% C, at an oxygen fugacity around IW-0.7 (Médard et al., 2008). Special care was taken that no Pt came into contact with this starting material and the Pt concentration in the reduced glass is below the detection limit of LA-ICP-MS (~4 ppb, Table 1).

2.2. Static experiments

Static experiments have been performed in 14.0 mm bore, end-loaded solid-medium piston-cylinder devices at ETH, at a constant pressure of 1.2 GPa and temperatures from 1360 to 2100 °C. A regular talc-Pyrex-graphite-MgO assembly has been used up to 1600 °C. For higher temperature experiments to 2100 °C, Pyrex was replaced by SiO₂-glass. The experimental samples were prepared by putting small clippings of high-purity Pt wire (99.95 %) at the bottom of a graphite container, and packing ~25-30 mg of basalt starting material on top. High-purity Fe metal or powdered Fe₂O₃ was also added together with the Pt in some experiments (Table 2). For experiments at 1360-1400 °C, the graphite container was encased in a Pt capsule that had been triple crimped, welded shut and flattened on one end. Graphite powder was packed above and below the graphite capsule, then the top of the outer Pt capsule was crimped and welded shut. No outer Pt capsule was used at ≥ 1600 °C. Capsules were fitted in an alumina sleeve and positioned in the hotspot of a straight-walled graphite furnace using MgO spacers. Pressure calibration based on the reactions coesite = quartz (Bose and Ganguly, 1995) and fayalite + quartz = ferrosilite (Bohlen et al., 1980) resulted in a 10% friction-correction for the talc-Pyrex assembly. No pressure calibration has been done for the talc-SiO₂ assembly; we assume a correction similar to the talc-Pyrex assembly. Pressures are thought to be accurate within ± 0.01 GPa, the oil pressure acting on the piston being held automatically within ± 0.2 bar during the entire experiment. Temperature was monitored using either type B thermocouples (Pt₉₄Rh₆-Pt₇₀Rh₃₀) to 1600 °C, or type C thermocouples (W₉₇Re₃-W₇₅Re₂₅) at ≥ 1700 °C, with no correction for the effect of pressure on thermocouple emf, and was controlled to within ± 2 °C of the setpoint using an Eurotherm controller. Temperatures are thought to be accurate within ± 10 °C. Experiments were pressurized at room temperature to 0.4 GPa, after which the temperature was raised at 50 °C/min to the target temperature. When temperature reached ~ 700 °C (for the Pyrex-bearing assembly) or ~ 1000 °C (for the SiO₂-glass assembly), pressure was raised to the target pressure and held constant. Experiments were terminated by shutting off heating power to the apparatus. Experimental conditions are presented in Table 2.

Three experiments (B1072, B1087 and B1092) already reported by Médard et al. (2008) were performed in a 12.7 mm bore piston-cylinder at MIT, using BaCO₃ assemblies. Another experiment (C1006) and syntheses of the reduced glass were run in a 19.1 mm piston-cylinder at LMV, Clermont-Ferrand, using salt/Pyrex assemblies and following the same experimental procedures than Médard et al. (2004).

2.3. *Dynamic experiments*

Dynamic experiments (Table 3) were run at ETH using a miniaturized 14 mm bore non-endloaded piston-cylinder mounted on a centrifuge (Ardia et al., 2008; Schmidt et al., 2006). This setup allows the experimental sample to be accelerated to 1500 g at a rotation of ~2000 rpm and a sample position at ~327 mm radius. The centrifugation increases the settling velocity of solid particles (for example metallic nuggets) present during the experiment such that Pt-nuggets of 0.1 μm diameter should settle at ~0.5 mm/h at 1500 g acceleration. Dynamic experiments are two stage experiments: a first static equilibration experiment is run in a regular endloaded piston-cylinder. The sample is then transferred into a new assembly and run in the centrifuging piston-cylinder at high acceleration. Assemblies, thermocouples, and temperature control are identical for the static and the centrifuging experiments.

Pressure can be monitored but not modified during centrifuging. A second limitation is posed by the fact that heating is only advisable when centrifuging (at a minimum of 200 rpm). The experiment is thus first pressurized to 0.4 GPa, heated at low acceleration to the temperature of glass softening (~ 700 °C for Pyrex, ~1000 °C for SiO₂ glass), quenched, pressurized to a target pressure lower than the final pressure to account for thermal expansion, and then simultaneously heated to the final temperature and brought to the final acceleration. This procedure can result in a significant deviation from the nominally desired pressure (Table 3).

2.4. *Major element analysis*

All experiments contain a silicate glass and a metallic bead (Fig. 1a). These were analyzed for major elements with the JEOL JXA-8200 electron microprobe at ETH. On-line data reduction was accomplished using the $\phi\rho Z$ correction procedure. For silicate glasses, a 10 nA beam current, 15 kV accelerating potential and 20 μm beam diameter were used for all analyses. Calibration was performed on natural and synthetic oxides and silicates. Metallic alloys were first analyzed using a 30 nA beam current, 15 kV accelerating potential, and 20 μm beam diameter, with pure Pt (M α line) and Fe (K α line) metals as standards. Many metallic alloys are liquid under experimental temperature and quench to a fine-grained, multi-phased mix (Fig. 1b). However, using a 20 μm defocused beam results in homogeneous individual analyses each representing average values of the liquid alloy composition.

Experimental alloys with low microprobe totals were re-analyzed with a procedure including carbon on the CAMECA SX-100 electron microprobe at LMV. Graphite-saturated cohenite (Fe_3C) was synthesized at 1.5 GPa and 1200 °C for 46 h in a graphite capsule (Tsuzuki et al., 1984) and used as a carbon standard, together with pure Pt and Fe metals. Walker et al. (2013) have shown that Fe_3C is non-stoichiometric: under conditions similar to our experimental conditions (1 GPa and 1210 °C), graphite-saturated Fe_3C contains 6.9 wt% C (25.7 at% C), compared to the stoichiometric value of 6.7 wt%. Since our alloys are conductive, carbon paint was carefully applied such that just the rim of the alloy was covered. This allows for charge transfer during the analysis (Chabot et al., 2008) but avoids carbon contamination. Carbon concentrations were analyzed on a PC2 spectrometer. Due to the presence of high order Pt L_α and Fe K_α peaks near the C K_α peak, the background correction was taken as the height of the C K_α peak for C-free standards (Fe and Pt), instead of the usual background measurements on both sides of the peak.

2.5. Platinum in glasses

Pt concentrations in silicate glasses were analyzed by LA-ICP-MS, using a Ti:sapphire femtosecond laser system (Legend, Coherent Inc., Santa Clara, CA, USA) on its fundamental wavelength, coupled to an Elan DRC II (PerkinElmer SCIEX, Thornhill, Canada) ICP-MS. The analytical conditions are given in Table 4. ^{178}Hf was measured to ensure that HfO interference on the Pt isotopes can be excluded since the natural starting material contained small amounts of Hf. The laser beam was focused using a plano-convex lens ($f = 75$ mm) and the focal point was kept slightly (~ 0.5 mm) below the sample surface. A cylindrical ablation cell with a volume of ~ 40 cm³ was used. For standardization, NIST 612 (2.59 ppm Pt) was used as external standard and ^{42}Ca as internal one, using the CaO concentration derived from the microprobe data. The concentrations of NIST 612 were taken from the GeoReM database (<http://georem.mpch-mainz.gwdg.de>, Jochum et al., 2005). Three major Pt isotopes (^{194}Pt , ^{195}Pt , ^{196}Pt) were analyzed and the three concentrations calculated from each isotope were averaged, since the variation in the three different measurements was lower than the one between different measurements. A minimum of three widely spaced spots were analyzed in each experimental sample.

3. Results

3.1. Experiments using natural starting material

Twenty-one experiments were performed on the natural basaltic starting material, with temperature varying from 1360 to 2100 °C and oxygen fugacity from $\Delta IW = -2.0$ to $+2.6$, where ΔIW^1 is the oxygen fugacity difference between the experiment and the iron-wüstite (IW) buffer (Campbell et al., 2009), expressed in log units. This variation in experimental oxygen fugacity was achieved by adding variable amounts of metallic Fe in addition to Pt (Grove, 1981; Médard et al., 2008). Fe_2O_3 powder was also added in a few experiments to maintain high oxygen fugacities. For a given temperature and pressure, there is a rough correlation between the composition of the added metal and the oxygen fugacity (Fig. 2). Oxygen fugacity can be tuned over 4 orders of magnitude, however, it is limited by two constraints: (1) at high oxygen fugacity, use of a graphite capsule forbids oxygen fugacities higher than that imposed by the graphite / CO / CO_2 equilibrium (i.e. the CCO buffer, Jakobsson and Oskarsson, 1994); and (2) the lowest possible oxygen fugacity that can be reached is when the metallic alloy does not contain any Pt (pure Fe with some dissolved C).

All experiments contain a homogeneous silicate glass of basaltic composition and a single bead of metallic alloy (Table 5). Depending on temperature and oxygen fugacity, two types of metallic alloys were analyzed: (1) at low temperature and high fO_2 ($> IW+0.1$ at 1400 - 1600 °C), solid alloy beads are homogeneous, have an oblong shape and do not contain any detectable amount of carbon (below the 0.06 wt% detection limit of the microprobe); (2) at higher temperature ($T > 1600$ °C) or lower oxygen fugacity, liquid alloy beads are perfectly spherical and quench to a dendritic intergrowth of phases variously enriched in Pt, Fe, and C. Carbon concentrations are always above detection limit. The composition of the crystalline alloy, present between 1360 and 1600 °C varies from X_{Fe} (molar $Fe/(Fe+Pt+C)$) = 0.30 to 0.54. This variation results from the starting material: those experiments with metallic Fe added have higher Fe-concentrations in the Pt-Fe alloy and lower oxygen fugacities. Liquid alloys, present in experiments between 1380 and 2100 °C (Fig. 1b), have an X_{Fe} of 0.71 to 0.80 for those experiments where metallic Fe was added, and a X_{Fe} of 0.48-0.59 for those without added Fe or with Fe_2O_3 added. In the experiments at 1380-1400 °C a liquid results when metallic Fe was added causing > 66 wt% Fe in the alloy, contrasting solid alloys that have < 26 wt% Fe. At 1600-1700 °C the transition between solid and molten alloy is between

¹ The formulation developed by Campbell et al. (2009) gives the oxygen fugacity of the Fe-FeO equilibrium, hereafter referred to as iron-wüstite (IW) buffer in the paper. Under the pressures and temperatures investigated here, wüstite is however non-stoichiometric, and the real equilibrium between iron and wüstite (O'Neill, 1988) is located on average 0.5 log unit higher than the Campbell IW reference used in our paper.

19 and 22 wt% Fe. The metallic melt contains between <0.5 and 4.5 wt% C, decreasing with increasing Pt-content. Analysis of quenched dendritic liquid alloys results in higher uncertainties than for solid alloys, particularly for C, with the analytical dispersion often reaching 0.5 wt% C, despite a 0.06 wt% detection limit. For Pt-rich liquid alloys with less than 50 wt% Fe, C concentrations are lower than 0.5 wt%, with a 2σ relative error around 100% (Table 5). Setting those values to zero (i.e. neglecting the effect of carbon) results in less than 6% relative error on fO_2 and partition coefficients.

Most experimental glasses show flat LA-ICP-MS time-resolved Pt spectra (Figs. 3a, 4b). Spikes, indicative of the presence of nanonuggets (Ertel et al., 2008), are only observed in a few samples, often at the edges. When present, the few spikes can easily be avoided when processing the LA-ICP-MS signal. Pt concentrations in all experimental glasses are constant throughout most of the experimental charge. This is unlike previous studies on Pt solubility at low fO_2 (Ertel et al., 2006), and will be discussed in the next section.

3.2. Attainment of equilibrium – reversal experiments

The natural starting material contains some amount of Fe^{3+} , and is likely more oxidized than all of the final experimental products. Our experiments with natural starting material are thus all reduction experiments. Since Pt partitioning is strongly fO_2 sensitive (at least at $fO_2 > IW+3$, Ertel et al., 1999), a progressive decrease in oxygen fugacity during the experiment could result in an overestimation of Pt concentration if equilibrium were not completely reached. Reversal experiments use a reduced starting glass ($\log fO_2 = -10.6 = IW-0.7$) that is oxidized during the experiments. Four reversal experiments were performed at temperatures between 1400 and 1900 °C (Table 2). Experimental run products are identical to the run products using the natural starting material. No evidence for Pt nuggets has been found in these experiments. Pt concentrations in reversal experiments are within the range of Pt concentration in regular experiments with natural starting material, indicating that equilibrium was achieved in all experiments. Partition coefficients (section 5) are almost identical in experiments run under similar conditions using the reduced and the natural starting material: at 1400 °C, they differ by less than 0.2 log units between experiments C1006 and Z164; at 1600 °C, they differ by 0.5 log units between experiments B966 and B786, and at 1900 °C they differ by 0.2 log units between experiments B967 and B816. Also the results of these reversal experiments indicate that equilibrium Pt concentrations were obtained in all of our experiments.

3.3. Nuggets production by Pt oversaturation

All the above experiments did not produce nanonuggets. To test the hypothesis that nanonuggets may form by Pt oversaturation, as suggested by Fortenfant et al. (2006) for Os, and Bennett et al. (2014) for Pt, two experiments at 1360-1400 °C (B1087 static and Z300 dynamic) were performed with an oxidized starting material that was enriched in Pt (Table 1, Table 2). The two experiments yielded silicate glasses in equilibrium with a solid Pt-rich alloy with ~12 wt% Fe. As will be discussed below, the static experiment yielded charges full of nanonuggets, whereas nanonuggets have been partially removed in the dynamic experiment. These two experiments are useful to elucidate the origin of nanonuggets but cannot be used to determine Pt partitioning.

Two main aspects of the data will be discussed in the following. First we will demonstrate that nanonuggets are high-temperature equilibrium metallic particles, whose formation depends on the experimental oxygen fugacity path. We will then investigate the parameters influencing the partitioning of Pt between silicate melt and metallic alloys, and show that temperature is the dominant factor that controls partitioning.

4. Pt in silicate melts: the nanonuggets issue

From our experiments and a review of the literature, it results that the nugget-issue contains two qualitatively different aspects: the formation of μm -sized Fe-rich microspheres and that of true Pt-rich nanonuggets. These aspects are discussed separately below.

4.1. High-temperature iron microspheres

Our higher temperature experiments (from 1800 °C to 2100 °C) contain μm -sized metallic spheres (Fig. 4a). These particles are clearly distinct from the nanonuggets of Ertel et al. (2008), and, in the following, the term “microspheres” will be used to distinguish them from “true” nanonuggets. The size of the microspheres is a rough function of temperature, the largest ones (up to 2 μm) being observed in run B868 at 2100 °C (Fig. 4a). Electron microprobe analyses indicate that the microspheres are made of pure Fe-metal, with Pt

concentrations below the detection limit (< 0.1 wt%). They are thus not equilibrium particles, as the equilibrium metallic alloys contain significant amounts of Pt (e.g., 35.9 wt% Pt in experiment B868, Table 4) and have Fe activities much lower than unity.

In experiment B868, the 2D-microsphere density can be estimated from SEM electron backscatter images at about $250 / \text{mm}^2$. The average diameter of the spheres is $1.7 \mu\text{m}$, so all the observed spheres have their centers inside a $1.7 \mu\text{m}$ thick slice of glass centered on the exposed surface. We thus conclude that the 3D-microspheres density is about $250 / 0.0017 = 15 \cdot 10^4 / \text{mm}^3$. With an average crater diameter of $150 \mu\text{m}$, and an average depth of $100 \mu\text{m}$, about 1000 microspheres should have been ablated during the 30 s of a LA-ICP-MS analysis. However, due to very low Pt concentrations in the microspheres, there is no visible change in the time-resolved Pt-concentrations (Fig. 4b), contrasting with the observations made on true low-temperature nanonuggets (Ertel et al., 2008).

These microspheres show strong similarities with the “micronuggets” of Cottrell and Walker (2006). Both experimental sets use relatively oxidized natural starting materials and similar capsule material and experimental conditions. In our experiments, microspheres are distributed in the entire glass area, whereas Cottrell and Walker (2006) describe a band of “micronugget”-free glass near the sides of their graphite capsules. This is, however, not obvious from their pictures (Fig. 2B), where “micronuggets” are also attached to the sides of the graphite capsule. Such an indication of heterogeneous nucleation is clearly visible in our experiments, where microspheres have a tendency to form at the sides of the graphite capsule, or on pieces of graphite dispersed in the experimental glass (Fig 4c).

In summary, microspheres (1) are observed in experiments at very high-temperature (at or above 1800°C), (2) have a different composition than the equilibrium metal (but their composition may reflect the Fe/Pt ratio of the glass), and (3) their presence has no influence on the Pt concentration in the silicate melt. We thus conclude that these microspheres are formed upon quench, and were not present during the experiment as equilibrium metallic particles. Microspheres may have been formed by a smelting reaction, as suggested by Cottrell and Walker (2006).

4.2. Nanonuggets-free experiments

With the exception of a few occasional spikes in Pt ablation-spectra near the edge of some samples (which could result from artefacts, see below), no evidence for Pt-bearing nanonuggets was found in our experiments performed with natural starting material. Metal-

silicate equilibration experiments on Pt (and other HSE) can be separated in two categories: (1) solubility experiments, where the metallic phase is pure Pt, equilibrated with a Fe-free silicate melt, often with bulk silicate compositions corresponding to the Di-An eutectic (Borisov and Palme, 1997; Ertel et al., 1999; Ertel et al., 2006; Fortenfant et al., 2003), and (2) partitioning experiments, where Pt-bearing metallic Fe is equilibrated with an Fe-bearing silicate melt (Bennett et al., 2014; Cottrell and Walker, 2006; Holzheid et al., 2000; Mann et al., 2012). Nanonuggets have been encountered in all solubility studies using Fe-free systems. They disappear at the highest temperatures and oxygen fugacities, and are increasingly more common towards low temperatures and oxygen fugacities. However, our experiments do not contain any nanonuggets, even at low temperatures (down to 1360 °C) and low concentrations (down to ~10 ppb). Our data are identical to the average lowest Fe-free data of Ertel et al. (2006) under similar conditions ($P = 1.0\text{--}1.5$ GPa, $fO_2 \sim \text{CCO}$ buffer), nevertheless without a need for nanonugget filtering. This strongly suggests that Fe plays a key role in nanonuggets formation/dissolution. The absence of nuggets in Fe-bearing versus Fe-free systems is in agreement with the results obtained by Laurenz et al. (2010) on Pd.

Dynamic experiments have been performed in order to ensure that our experiments were truly nanonugget-free. The average diameter of nanonuggets can be estimated to be between 50 nm and 1 μm (Ertel et al., 2008; Ertel et al., 1999; Fortenfant et al., 2006). Assuming that Stokes' law can be applied to such small particles, a calculated particle density of 18 $\text{g}\cdot\text{cm}^{-3}$ ($\text{Pt}_{75}\text{Fe}_{25}$ alloy) and a basalt density and viscosity of 2.9 $\text{g}\cdot\text{cm}^{-3}$ and 1 $\text{Pa}\cdot\text{s}$ (at 1400 °C, Giordano et al., 2008) lead to settling rates of the nanonuggets between 0.1 and 30 $\mu\text{m}\cdot\text{h}^{-1}$. By using a centrifuging piston-cylinder, settling rates can be multiplied proportionally to the g-force applied such that complete segregation of nanonuggets from the silicate melt can be reached within a few hours (settling velocities between 150 and 45 000 $\mu\text{m}\cdot\text{h}^{-1}$ at 1500 g). Experiment Z164, centrifuged at 1500 g for 11 hours results in a very homogeneous capsule interior, with possible evidence for nanonuggets only on the rims of the sample. Using only the interior spots, Z164 results within error in the same Pt concentration than the corresponding static experiment (37 ± 5 ppb instead of 33 ± 4 ppb for experiment B1072). The centrifuging should have moved even the smallest nanonuggets by more than a millimeter; hence nanonuggets did not form in experiments with the natural starting material. The presence of Pt spikes near the edges of samples, also observed in static experiments, may result from a preferential nucleation of nanonuggets near the graphite-silicate melt interface or by submicroscopic Pt impurities caught during polishing between the soft graphite and the

silicate glass and are judged to represent artefacts. Overall, no difference was observed between static and dynamic experiments using the natural starting material, strongly indicating that nanonuggets were not present during these experiments.

4.3. Formation and resorption of Pt-rich nanonuggets

Experiment B1087, using the Pt-rich oxidized starting material, produces an extremely nugget-rich charge, in which an equilibrium Pt concentration in between the nuggets cannot be measured (Fig. 3b). As in experiments with natural starting material, the oxygen fugacity is reduced through reaction between the silicate glass and the graphite capsule until reaching equilibrium near the CCO oxygen buffer. The only differences between the two types of experiments are the higher initial oxygen fugacity in the oxidized starting glass, and the Pt concentration in the starting glass: the oxidized starting glass, Pt-saturated in air, contains 3.2 ppm dissolved Pt (Table 1), whereas the natural glass contains a very low amount of Pt (below 4 ppb, Table 1). It is thus likely that nanonuggets formed from the Pt-rich material as a consequence of Pt-oversaturation during reduction, since Pt solubility is strongly dependent on oxygen fugacity at moderate to high fO_2 (at least above CCO, Borisov and Palme, 1997). It should be noted that for all experiments in which nuggets have been encountered, the final experimental fO_2 is systematically lower than the initial fO_2 of the starting material: (1) in CMAS experiments, the starting material is a glass synthesized in air (Amossé and Allibert, 1993; Borisov and Palme, 1997; Ertel et al., 1999; Ertel et al., 2006; Fortenfant et al., 2003), and (2) experiments in Fe-bearing systems (e.g., Cottrell and Walker, 2006) used natural starting materials, which likely contain small amounts of Fe^{3+} . Since equilibrium Pt concentrations are very small, any Pt that is present in the glass at the beginning of the experiment, or that dissolves in the glass at the initially high oxygen fugacity will result in Pt-oversaturation in the silicate melt at equilibrium, and hence in subsequent precipitation of equilibrium nanonuggets. Comparison between experiments using the natural, Pt-poor, starting material, and experiments using Pt-enriched starting material confirm that nanonuggets are equilibrium particles formed through oversaturation of the silicate melt upon reduction.

Once formed, nanonuggets can only be removed by two different mechanisms: physical segregation or Ostwald ripening. Nanonuggets that formed in the experiment using the Pt-bearing oxidized starting glass did not settle by gravity, even after 72 hours. The experiment

was duplicated with an equilibration time of 48 h, then centrifuged for 7h at 1000 g to remove the nanonuggets (experiment Z300, Table 3). According to Stokes' law, a 50 nm diameter nanonugget should have moved by at least 0.5 mm during the experiment. Time-resolved LA-ICP-MS analyses of experiment Z300 are presented in Fig. 5. In the static experiment B1087, Pt concentrations are highly variable, but on average similar to the initial Pt concentration of the starting material, and well above the equilibrium concentration. Concentrations in the dynamic experiment Z300 are on average significantly lower, with no spot above the initial concentration of the starting material (Fig. 5). They are, however, at least one order of magnitude above the expected equilibrium concentration. The minimum concentration measured in experiment Z300 is 150 ppb, compared to 19-37 ppb in equilibrium experiments under similar conditions, and > 1000 ppb in experiment B1087. These results indicate that nanonuggets were partially removed by centrifuging, but less than would be expected for 50 nm diameter particles obeying Stoke's law. It is possible: (1) that nanonuggets in our experiment are smaller than 50 nm. This value was proposed for example by Ertel et al. (1999), but if nanonuggets formed by oversaturation, their size should depend on the initial Pt concentration, the diffusion rate of Pt (i.e. the temperature) and the amount of oversaturation. Smaller nanonuggets could be present in our experiment, which is characterized by extreme oversaturation and low temperature (1400 °C); (2) that Stokes' law does not fully apply to such small particles; (3) that the settling of nanonuggets is hampered by small temperature gradients in the experiment which could induce a convective flow in the sample. Even if smaller than expected, the evidence for physical segregation demonstrate that nanonuggets can be formed by oversaturation and removed by physical processes.

Assuming that nanonuggets are formed during the experiments as a result of a local Pt oversaturation in the melt, the only driving force to remove them is interfacial energy minimization, resulting in Ostwald ripening: growth of the large metal beads at the expense of smaller nanonuggets. After formation, nanonuggets will be eliminated in a 3-step process: (1) detachment of a Pt atom from the metallic nugget and dissolution into the silicate melt, (2) diffusion of Pt in the silicate melt, and (3) attachment of the Pt atom to a larger equilibrium metal phase. When equilibrium Pt solubilities in the silicate melt are very low, diffusion represents the limiting step, as only a very small number of Pt atoms are dissolved and may diffuse at any given time. The lower the equilibrium concentration, the higher the chances of preserving nanonuggets, as observed in all previous experimental studies (e.g., Ertel et al., 2008). Nanonuggets could then in theory form through oversaturation with any transition

element, in experiments where the oxygen fugacity decreases during the experiment. The lower the element concentration in the silicate melt, and the lower the diffusion coefficient, the more difficult it will be to remove nanonuggets during an experiment. This would explain why nanonuggets are mainly encountered with the least soluble elements (the HSE), at their lowest possible concentrations (i.e., low T and low fO_2). If Pt is dissolved in an ionic form (Pt^{2+} or Pt^- , see below), step (1) requires an oxidation or a reduction of Pt^0 . This redox reaction can only proceed in the presence of a redox partner, e.g. other multiple valence elements like Fe. This key role would explain the rarity of nanonuggets in Fe-bearing experiments compared to Fe-free experiments.

5. Pt-partitioning between metal and silicate

5.1. Activity models

Nernst partition coefficients, calculated from measured mass or molar concentrations are only useful at low concentrations where Henry's law is valid. To account for the large range in experimental FePt-alloy compositions, and in order to apply the experimental data on Pt-rich alloys to the low Pt concentrations relevant to core formation processes, we use partition coefficients based on activities:

$$D_{Pt}^{metal / silicate} = \frac{a_{Pt}^{metal}}{a_{Pt}^{silicate}}$$

This approach requires the calculation of activity coefficients for Pt in alloys and in silicate melts. For silicate melts, Pt concentrations are always <1 ppm, and activities are assumed to be proportional to concentrations according to Henry's law (the value of the constant h will be set to 1 in the following):

$$a_{Pt}^{silicate} = h \cdot X_{Pt}^{silicate} \quad (1)$$

For solid alloys, an activity model in the Pt-Fe system at 1200 – 1400 °C has been proposed by Kessel et al. (2001). Their asymmetric regular solution model was used here, and is in good agreement (maximum deviation 25 %) with the values at 1375 °C given by Franke and Neuschütz (2005). Comparison between solid alloy data from Kessel et al. (2001) and data for the liquid phase (Franke and Neuschütz, 2005) at 1775 °C show similar X-a relations for high Pt concentrations ($X > 0.5$), but slight differences at low concentrations, with relatively higher

activities of Pt (for a given X) in the liquid alloy. Indeed, liquid alloys are expected to be closer to ideality than solid alloys, i.e. activity coefficients are expected to be closer to unity. A model for the liquid Pt-Fe alloy was thus constructed by fitting an asymmetric regular solution model to the activity data of Franke and Neuschütz (2005).

The use of graphite capsules provided a source of carbon that may dissolve in the Pt-Fe alloy. This effect is negligible for solid alloys due to the very low solubility of carbon in Pt (Watson, 1987), and because all investigated solid alloys are Pt-rich. However, liquid alloys can contain large amounts of dissolved carbon (up to 4.5 wt%, Table 5). For the Pt-Fe-C liquids, a ternary asymmetric regular solution model was constructed after Andersen and Lindsley (1981), assuming pressure-independent Margules parameters and no ternary interaction components. Margules parameters were obtained by fitting asymmetric regular solution models to the data of Franke and Neuschütz (2005) for the three individual binaries (Pt-Fe, Pt-C and Fe-C), following the same approach as Mann et al. (2012). Margules parameters include a temperature dependency to account for the large range of investigated temperatures:

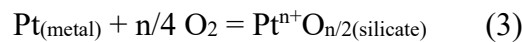
$$W_G = W_H - TW_S \quad (2)$$

$$W_H^{FePt} = -267.6 \text{ kJ.mol}^{-1}, W_H^{PtFe} = -205.6 \text{ kJ.mol}^{-1}, W_H^{PtC} = 228.3 \text{ kJ.mol}^{-1}, W_H^{CPt} = 100.4 \text{ kJ.mol}^{-1}, \\ W_H^{FeC} = 93.2 \text{ kJ.mol}^{-1}, W_H^{CFe} = -23.7 \text{ kJ.mol}^{-1}$$

$$W_S^{FePt} = W_S^{PtFe} = -72.0 \text{ J.mol}^{-1}.K^{-1}, W_S^{PtC} = 24.6 \text{ J.mol}^{-1}.K^{-1}, W_S^{CPt} = 51.5 \text{ J.mol}^{-1}.K^{-1}, \\ W_S^{FeC} = W_S^{CFe} = 0$$

5.2. Pt valence in silicate melts

The dissolution of metals in silicate melts is often assumed to occur through formation of a metal oxide. The valence of a dissolved metal can then be estimated from the partitioning as a function of oxygen fugacity as follows (e.g., Borisov et al., 1994):



where n is the valence of dissolved Pt. The equilibrium constant of this reaction is given by:

$$K = \frac{a_{\text{PtO}_{n/2}}^{\text{silicate}}}{a_{\text{Pt}}^{\text{metal}} \cdot f_{\text{O}_2}^{n/4}} = \frac{1}{D_{\text{metal/silicate}}^{\text{Pt}} \cdot f_{\text{O}_2}^{n/4}} \quad (4)$$

By plotting the partition coefficient as a function of oxygen fugacity, all other parameters (temperature, pressure, melt composition) being kept constant, one can solve for the valence of dissolved Pt. Oxygen fugacity in the experiments was derived from Fe partitioning between silicate melt and metal, using the model proposed by Médard et al. (2008). This experimentally calibrated model only accounts for solid Pt-Fe binary alloys. For experiments containing a liquid ternary Fe-Pt-C alloy, an analogous model was used, where the solid alloy activity model was replaced by the asymmetric regular solution model described in part 5.1.

Log/log plots of partition coefficients as a function of oxygen fugacity for three different temperatures (1400 °C, 1600 °C, and 1900 °C) are presented in Fig. 6, together with literature data and their extrapolations at similar temperatures (Bennett et al., 2014; Borisov and Palme, 1997; Ertel et al., 2006; Fortenfant et al., 2003). All three datasets indicate that, for oxygen fugacities below $\sim 10^{-6}$, as investigated here, Pt partition coefficients remain constant or decrease with decreasing oxygen fugacity. Hence, Pt would be dissolved in the metallic state as Pt^0 ($n = 0$) or anionic Pt^- ($n = -1$). The presence of zero-valence Pt in silicate melts at low oxygen fugacity was initially suggested by early experimental studies on Pt solubility (Amossé and Allibert, 1993), but these data were not reproduced by subsequent studies. Other early studies suggesting the presence of neutral metals in silicate melts (e.g., Colson, 1992; O'Neill et al., 1995) were widely discarded, and the leveling of solubility at low oxygen fugacity was interpreted as a consequence of the presence of nanonuggets (e.g., Ertel et al., 2008). The only evidence for zero-valence metal in silicate melt published so far is for Pd (Borisov et al., 1994), although the samples were analyzed by bulk methods (neutron activation), such that the presence of nanonuggets would go undetected. For Pt, the most recent studies at 1 atm indicate that it dissolves as Pt^{2+} down to at least $f_{\text{O}_2} = 10^{-5}$ at 1400 °C (Borisov and Palme, 1997; Ertel et al., 1999). Experiments at lower oxygen fugacity could not be used for quantification due to the presence of nanonuggets (Fig. 6). Our experiments at ~ 1400 °C suggest that Pt could be dissolved as Pt^0 for f_{O_2} lower than $f_{\text{O}_2} = 10^{-7}$ ($\sim \Delta \text{IW} + 3$). The transition between Pt^{2+} and Pt^0 would occur at slightly higher absolute oxygen fugacities at higher temperatures (Fig. 6). Our data are equally consistent with a negative valence for dissolved Pt (Pt^-), particularly at 1900 °C below $f_{\text{O}_2} = 10^{-6}$ (Fig. 6). A similar trend is shown

by the 2000 °C data of Bennett et al. (2014) at even higher fO_2 (Fig. 6). Platinide anions (Pt^- and Pt^{2-}) are stabilized by the strong contraction of the 6s orbital of Pt (Jansen, 2005). They have already been observed in a few ionic compounds (e.g., Karpov et al., 2006), and can thus possibly be stable in silicate melts.

As discussed above, evidence for nanonuggets is absent in our experiments, except for those starting from the Pt-rich heavily oxidized material, which are not used for the partitioning model. In most experiments, the relatively oxidized (natural) starting material reacts with the added Pt (and Fe) metal and the graphite capsule, resulting in a decrease in absolute oxygen fugacity. Instead, reversal experiments using a reduced starting material are characterized by an increase in absolute oxygen fugacity during the experiment. Pt oversaturation can thus not occur in these experiments. The four reversal experiments give similar results (e.g., Fig. 7) to the equivalent regular experiments, indicating that all of our experiments have indeed reached equilibrium. In previous studies, the loss of correlation between fO_2 and Pt (or other HSE) concentrations at low fO_2 has been taken as an indication of disequilibrium due to the presence of nanonuggets (e.g., Borisov and Palme, 1997; O'Neill et al., 1995). Such a feature can indeed be explained if the lowest fO_2 experiments initially equilibrated at higher fO_2 , and the higher Pt concentration failed to re-equilibrate when the oxygen fugacity decreased. The constant Pt solubility below a certain oxygen fugacity would then be an indication of the concentration level below which diffusive re-equilibration becomes too slow to provide equilibrium concentrations within experimental time frames. However, in our experiments, the measured Pt concentrations in the melt do not level out at low oxygen fugacity, but are highly correlated with fO_2 , as observed in solubility studies at higher fO_2 (Fig. 7). This strong variation in Pt concentration in the silicate melt is paralleled by a change in composition of the metallic alloy, resulting in a constant or even decreasing partition coefficient.

The evidence for equilibrium demonstrates that the loss of a correlation between partition coefficient and oxygen fugacity in our experiments cannot be explained by a disequilibrium process, and clearly indicates that at oxygen fugacities relevant for core formation, Pt is indeed dissolved as a neutral species, or even anionic (Pt^-). Progressive decreases in valence with decreasing oxygen fugacity have been observed with many other HSE (e.g., Bennett and Brenan, 2013; Ertel et al., 2008), although Pt was so far an exception.

5.3. Possible platinum speciation in silicate melts at low oxygen fugacity ($< IW+3$)

The coordination environment of the Pt dissolved in the silicate melt at low fO_2 cannot be constrained from our experiments. Studies arguing for the presence of dissolved metals as neutral atoms (Borisov et al., 1994; Colson, 1992) are controversial. Another option is the presence of Pt complexes: at the extremely low Pt concentrations observed in our experiments, many other trace elements are orders of magnitude more abundant and are available for the formation of coordination complexes. We show below that Pt complexes are unlikely, and that dissolution of Pt atoms or Pt^- anions in the silicate melt is the most likely mechanism to explain the observed constant or decreasing partition coefficient.

Since our experiments have been performed in graphite capsules, the presence of neutral or negatively-charged Pt-carbonyl or Pt-carbide complexes (Borisov and Palme, 1996; Ertel et al., 1999) could explain the observed oxygen fugacity behavior. Recent experimental studies of carbon solubility in silicate melts at low oxygen fugacity indeed suggest that metal-carbonyls could become dominant species (Fe-carbonyls, Stanley et al., 2014; Wetzel et al., 2013). However, work by Bennett et al. (2014) showed no correlation between the carbon content of the melt and the Pt concentration at low oxygen fugacity, as would be expected if the dissolution reaction involved carbon.

Likewise, sulfur has been shown to have a strong influence on Pd partitioning (Laurenz et al., 2013), and small amount of sulfur could drastically change Pt behavior during core formation. Trace amounts of sulfur are likely present in our natural starting material. Sulfur, however, is an unlikely species in the synthetic starting material. The fact that partition coefficients are identical in experiments run with the natural and the synthetic starting material (e.g., Fig. 7) indicate that sulfur as a ligand will not explain the behavior of Pt in our experiments.

Silicon is another potential ligand for Pt complexes. The presence of Au silicides has been proposed by Borisov and Palme (1996). The formation of a Pt silicide is an oxygen-producing reaction (Bennett et al., 2014), and would thus result in an increase in solubility with decreasing oxygen fugacity. However, silicides are only stable at $fO_2 < IW-5$, much lower than our experimental range (e.g., Schmidt et al. 2014).

5.4. Temperature dependence

Since all our experiments have been performed at roughly constant pressure (~ 1.2 GPa) and constant melt composition, and assuming that oxygen fugacity has no effect on partition coefficients below IW+3 (zero valence), our experiments can be used to quantify the effect of temperature on silicate/metal Pt-partitioning. Fortenfant et al. (2003) and Ertel et al. (2006) have shown that Pt solubility increases (and thus Pt partitioning decreases) with temperature. Regression of our entire partitioning dataset (21 data points, Fig. 8a) as a function of inverse temperature gives a correlation coefficient of 0.922. This high correlation coefficient confirms the robustness of our experimental data. If we consider the possibility of an influence of oxygen fugacity (-1 valence), and only use the results within a restricted range of oxygen fugacity (for example, $-6.5 > \log fO_2 > -7.5$, 11 data points, Fig. 8a), the correlation coefficient is improved (0.941) but the correlation does not change significantly. In the following discussion, we thus use the temperature trend based on all the data.

Partition coefficients have a similar slope versus temperature than that calculated from the nanonugget-filtered data of Ertel et al. (2006), and both dataset predict similar results (Fig. 8b). The small difference can be ascribed to the large uncertainty introduced by the necessary nanonugget-filtering in Ertel's low-temperature data. Part of the difference could also be due to a known effect of Fe on HSE partitioning (Laurenz et al., 2010), since the experiments of Ertel et al. (2006) were performed in an iron-free system. Our data are also consistent with the higher pressure Fe-bearing data of Mann et al. (2012) and Bennett et al. (2014). All of these datasets are, however, inconsistent with the experimental dataset of Cottrell and Walker (2006). Their experimental conditions broadly overlapped with ours (oxygen fugacities of IW-1.2 to IW-5.4 at 1940-2500 °C compared to IW-0.4 to IW-2 at 1800-2100 °C in our highest temperature experiments), but the results are different by at least two orders of magnitude (Fig. 8b). The reason for this discrepancy is still unknown, but could possibly be related to the hidden presence of nanonuggets in their experiments.

To test for the possible influence of oxygen fugacity, the entire existing partitioning database has been plotted by oxygen fugacity range in Fig. 8c. No significant trend is visible, although there is a tendency for lower oxygen fugacity experiments to produce lower partition coefficients. This tendency would be in agreement with the possible occurrence of anionic dissolution mechanisms at the lowest oxygen fugacities, as suggested by the 2000 °C data of Bennett et al. (2014) and our 1900 °C data. If this was the case, however, considering that our highest temperature experiments (1800-2100 °C) have an average oxygen fugacity of IW-1.2, and considering that Pt is dissolved as a (-1) species (Fig. 6), a decrease of one order of magnitude in partition coefficient will require a decrease in oxygen fugacity by four orders of

magnitude (see 5.2.), down to IW-5.2. Note that Cottrell and Walker (2006) data all plot at lower partition coefficients, irrespective of their oxygen fugacity.

5.5. Influence of pressure and silicate melt composition

The influence of pressure has not been investigated in our study, since all experiments have been performed in the narrow pressure range of 0.7 to 1.6 GPa. A previous study by Ertel et al. (2006) has shown that pressure has a negligible effect on Pt solubility to at least 16 GPa. Comparison of our data with the datasets of Ertel et al. (2006) at 0.5-16 GPa and Mann et al. (2012) at 3.5 - 18 GPa (Fig. 8b) confirms this finding. An insignificant effect of pressure has also been reported for Pd and Re partitioning (Bennett and Brenan, 2013; Holzheid et al., 2000).

Borisov and Danyushevsky (2011) have shown that changes in silica content have a small influence on Pt solubility. Nevertheless, significant variations were only observed when approaching geologically non-significant silica-free oxide melts. A comparison between our basaltic melts and the peridotitic melts of Mann et al. (2012) does not show any significant difference (Fig. 8b). Moreover, one of our experimental capsules leaked, and the silicate melt was contaminated by the surrounding MgO and Pyrex (experiment Z184): the MgO-content is twice as high as in the starting material and the analytical total of 90 wt% for the resulting silicate glass can be explained by significant quantities of B₂O₃. Despite the different glass composition, partitioning results for this experiment are very similar to those obtained in regular experiments. All these observations suggest that major element composition of the melt has an insignificant influence on Pt partitioning, and that temperature is by far the most important factor.

6. Implications for core formation models

6.1. Pt partitioning at infinite dilution

Early determinations of equilibrium Pt partitioning during core formation were based on extrapolations of atmospheric pressure data at temperatures < 1600 °C (Borisov and Palme, 1997; Ertel et al., 1999; Fortenfant et al., 2003), assuming that Pt dissolves as Pt²⁺ regardless of oxygen fugacity. 1 atm experimental data yielded metal/silicate partition coefficients for

oxygen fugacities relevant to core formation around 10^9 . With such partition coefficients, the Earth's mantle should have been quantitatively stripped of Pt during core formation. The presence of small but significant amounts of Pt in the mantle (around 0.006 times the chondritic value, Becker et al., 2006) can only be reconciled with equilibrium partitioning if one considers late addition of Pt-bearing material that did not equilibrate with the core (the so-called “late-veneer”).

Our experiments in combination with available literature data suggest that, at the low oxygen fugacities relevant for core formation processes ($fO_2 < IW+2$), Pt dissolves as neutral or negatively charged species. Extrapolations based on Pt^{2+} thus strongly overestimate partition coefficients. Our data, as well as those of Ertel et al. (2006), Mann et al. (2012), and Bennett et al. (2014) indicate that temperature is the only significant parameter influencing Pt partitioning in a relatively reduced Earth. Regression of the data in Fig. 8a gives the following temperature dependence of the activity-based partition coefficient D:

$$\log D_{Pt}^{metal / silicate} = 0.9396 + 10501/T \quad (5)$$

Assuming temperature and pressure-independent Margules coefficients for Pt in liquid Pt-Fe alloys and using the activity data of Franke and Neuschütz (2005), we can derive the activity coefficient for Pt in metallic iron melt at infinite dilution:

$$\log \gamma_{Pt}^{\infty metal} = -2844/T \quad (6)$$

Note that this value is for liquid metal, and significantly lower than the one used for solid metal; if extrapolated down to 1300 °C, the activity coefficient is $1.6 \cdot 10^{-2}$, compared to $3 \cdot 10^{-5}$ in solid metal (Gudmundsson and Holloway, 1993). From this, one can derive the concentration-based partition coefficient D^* for Pt at infinite dilution (in mole fraction):

$$\log D_{Pt}^{* metal / silicate} = 0.9396 + 13345/T \quad (7)$$

A mass-based partition-coefficient can be obtained by taking into account the molar weight of the metallic core (assumed to be pure iron, $M = 55.85 \text{ g.mol}^{-1}$) and the average molar weight of mantle-forming oxides ($M = 50.71 \text{ g.mol}^{-1}$ for Hart and Zindler, 1986, composition). Since both molar weights are similar, the result is almost identical to the mole-based partition coefficient. The commonly used, mass-based Nernst partition coefficient between metal and silicate liquids at infinite dilution is expressed by:

$$\log D_{Pt}^{M metal / silicate} = 1.0348 + 14698/T \quad (8)$$

When extrapolated to a core-formation temperature of 3300 K (Bouhifd and Jephcoat, 2011; Righter, 2011), metal/silicate partition coefficients from Eq. (8) are around 10^5 - 10^6 . Values that explain the abundance of Pt in the mantle by equilibrium core formation models

are around 10^2 , three orders of magnitude lower than the experimental values. By varying the equilibrium temperature within reasonable bounds, $\log D$ varies from 6.9 at 2500 K to 4.7 at 4000 K, still well above 2. Even if Pt was dissolved as a (-1) species at low oxygen fugacity, a decrease of D by two orders of magnitude would require a decrease of the oxygen fugacity by 8 orders of magnitude. The average oxygen fugacity of our highest temperature experiments (1800-2100 °C), IW-1.2, is, however, similar to the conditions most likely to prevail at the end of Earth's accretion (IW-2, Wade and Wood, 2005). Thus, even if our results are orders of magnitude lower than previous determinations based on 1 atmosphere data, they confirm that equilibrium core/mantle partitioning cannot explain the observed HSE concentrations in the Earth's mantle, hence additional processes that increase the Pt concentration in the mantle are required.

6.2. *The mass of the late veneer*

Using a simple mass-balance equation, with the mass of the core making up 32.5 % of the total mass of the Earth, a chondrite-normalized Pt concentration in the mantle of 0.006 (mantle composition from Becker et al., 2006; average of all chondrite compositions measured by Horan et al., 2003), and an equilibrium core-segregation temperature of 3300 K (as estimated from the partitioning of moderately siderophile elements, Bouhifd and Jephcoat, 2011; Righter, 2011), an extra 0.60 ± 0.03 wt % of chondritic material needs to be added to the Earth's mantle without sequestration of material to the core to explain the present day mantle composition. This value depends little on the Pt partition coefficient, indicating that any experimental uncertainties or further uncertainties during data reduction (i.e. the exact value of the activity coefficient of Pt in liquid Fe at infinite dilution) will not strongly change the amount of extra material required. The parameter that exerts the strongest control on the amount of late veneer is the ratio of the Pt concentration in the Earth's mantle to that of the added (late veneer) material. By varying this ratio between 0.005 and 0.01 (Becker et al., 2006; Palme and O'Neill, 2003), the amount of late veneer varies between 0.49 and 1.01 wt% of the Earth's mantle. These values are in excellent agreement with values derived from other HSE like Os, Ir and Re (about 0.5 wt% of late veneer, Bennett and Brenan, 2013; Brenan and McDonough, 2009). The calculated value of 0.60 wt% is, however, significantly lower than the amount of volatile-rich chondritic material required to explain the volatile content of the Earth by late veneer addition only (e.g., 2 ± 1 wt%, Marty, 2012). Note that we used a global average of chondrite compositions for our calculations. Selecting a particular set of chondrites

(carbonaceous chondrites, ordinary chondrites, enstatite chondrites) has a negligible influence on the result, except for two classes of carbonaceous chondrites (CI and CM), that contain up to 30% less Pt than the average chondrite (Horan et al., 2003). If the late veneer was of volatile-rich CI chondrites (e.g., Wang and Becker, 2013), our model gives a larger addition of 0.89 wt% of Earth's mantle, somewhat closer to the estimate of Marty (2012). A late veneer of CM chondrites (e.g., Wang and Becker, 2013) would amount to 0.72 wt% of Earth's mantle.

7. Conclusions

This study has evaluated the factors leading to the formation of micro- and nanonuggets in experiments and provides a recipe how to avoid these undesired features. Nanonuggets are present during experiments and result from oversaturation of the silicate melt during initial oxygen fugacity equilibration. True HSE partitioning data can be obtained without encountering the nanonugget problem through avoiding any Pt oversaturation of the silicate liquid in the course of an experiment. The true Pt partition coefficients (and by analogy of any other HSE metal) are generally close to the values derived from the lowest measured Pt concentrations at a given set of T-fO₂ conditions.

Our experimental data confirm that the Pt concentration of the Earth mantle cannot be explained solely by equilibrium metal/silicate partitioning, and requires the late addition of ~0.60 wt% chondritic material to the Earth after core segregation had completed. This late material thoroughly mixed with the mantle, but never equilibrated with the core.

Acknowledgments

P. Ardia and L. Martin helped with the centrifuge experiments, and J.-L. Devidal and J. Langlade with microprobe analyses. This paper benefited from reviews by D. Walker and N. Bennett, and comments by associate editor R. Dasgupta, as well as discussions with U. Mann, A. Bouhifd and J. Van Orman. This project was funded by the Swiss National Science Foundation. This is Labex Clervolc contribution number xxx.

Bibliography

Amossé, J., Allibert, M., 1993. Partitioning of iridium and platinum between metals and silicate melts: evidence for passivation of the metals depending on fO₂. *Geochimica et Cosmochimica Acta* 57, 2395-2398.

Andersen, D.J., Lindsley, D.H., 1981. A valid Margules formulation for an asymmetric ternary solution: revision of the olivine-ilmenite thermometer, with applications. *Geochimica et Cosmochimica Acta* 45, 847-853.

Ardia, P., Giordano, D., Schmidt, M.W., 2008. A model for the viscosity of rhyolite as a function of H₂O-content and pressure: a calibration based on centrifuge piston cylinder experiments. *Geochimica et Cosmochimica Acta* 72, 6103-6123.

Becker, H., Horan, M.F., Walker, R.J., Gao, S., Lorand, J.-P., Rudnick, R.L., 2006. Highly siderophile element composition of the Earth's primitive upper mantle: constraints from new data on peridotite massifs and xenoliths. *Geochimica et Cosmochimica Acta* 70, 4528-4550.

Bennett, N.R., Brenan, J.M., 2013. Controls on the solubility of rhenium in silicate melt: implications for the osmium isotopic composition of Earth's mantle. *Earth and Planetary Science Letters* 361, 320-332.

Bennett, N.R., Brenan, J.M., Koga, K.T., 2014. The solubility of platinum in silicate melt under reducing conditions: results from experiments without metal inclusions. *Geochimica et Cosmochimica Acta* 133, 422-442.

Bohlen, S., Boettcher, A., Dollase, W., Essene, E., 1980. The effect of manganese on olivine-quartz-orthopyroxene stability. *Earth and Planetary Science Letters* 47, 11-20.

Borisov, A., Danyushevsky, L., 2011. The effect of silica on Pd, Pt and Rh solubilities in silicate melts: an experimental study. *European Journal of Mineralogy* 23, 355-367.

Borisov, A., Palme, H., 1996. Experimental determination of the solubility of Au in silicate melts. *Mineralogy and Petrology* 56, 297-312.

Borisov, A., Palme, H., 1997. Experimental determination of the solubility of platinum in silicate melts. *Geochimica et Cosmochimica Acta* 61, 4349-4357.

Borisov, A., Palme, H., Spettel, B., 1994. Solubility of palladium in silicate melts: implications for core formation in the Earth. *Geochimica et Cosmochimica Acta* 58, 705-716.

Bose, K., Ganguly, J., 1995. Quartz-coesite transition revisited - reversed experimental determination at 500-1200 °C and retrieved thermochemical properties. *American Mineralogist* 80, 231-238.

Bouhifd, M.A., Jephcoat, A.P., 2011. Convergence of Ni and Co metal-silicate partition coefficients in the deep magma-ocean and coupled silicon-oxygen solubility in iron melts at high pressures. *Earth and Planetary Science Letters* 307, 341-348.

Brenan, J.M., McDonough, W.F., 2009. Core formation and metal-silicate fractionation of osmium and iridium from gold. *Nature Geoscience* 2, 798-801.

Campbell, A.J., Danielson, L., Richter, K., Seagle, C.T., Wang, Y., Prakapenka, V.B., 2009. High pressure effects on the iron-iron oxide and nickel-nickel oxide oxygen fugacity buffers. *Earth and Planetary Science Letters* 286, 556-564.

Carlson, R.W., Shirey, S.B., Schönbachler, M., 2008. Applications of PGE radioisotope systems in geo- and cosmochemistry. *Elements* 4, 239-245.

Chabot, N.L., Campbell, A.J., McDonough, W.F., Draper, D.S., Agee, C.B., Humayun, M., Watson, H.C., Cottrell, E., Saslow, S.A., 2008. The Fe-C system at 5 GPa and implications for Earth's core. *Geochimica et Cosmochimica Acta* 72, 4146-4158.

Chabot, N.L., Draper, D.S., Agee, C.B., 2005. Conditions of core formation in the Earth: constraints from nickel and cobalt partitioning. *Geochimica et Cosmochimica Acta* 69, 2141-2151.

Chou, C.-L., 1978. Fractionation of siderophile elements in the Earth's upper mantle. *Proceedings of the 9th Lunar and planetary science conference*, 219-230.

Colson, R.O., 1992. Solubility of neutral nickel in silicate melts and implications for the Earth's siderophile element budget. *Nature* 357, 65-68.

Cottrell, E., Walker, D., 2006. Constraints on core formation from Pt partitioning in mafic silicate liquids at high temperatures. *Geochimica et Cosmochimica Acta* 70, 1565-1580.

De Bruin, H., Tangtreeratana, M., 1981. Diffusion of palladium into MgO. *Journal of Physics and Chemistry of Solids* 42, 333-334.

Donnelly-Nolan, J.M., Champion, D.E., Grove, T.L., Baker, M.B., Taggart, J.E., Bruggman, P.E., 1991. The Giant Crater lava-field - Geology and geochemistry of a compositionally zoned, high-alumina basalt to basaltic andesite eruption at Medicine Lake Volcano, California. *Journal of Geophysical Research* 96, 21843-21863.

Ertel, W., Dingwell, D.B., Sylvester, P.J., 2008. Siderophile elements in silicate melts - a review of the mechanically assisted equilibration technique and the nanonugget issue. *Chemical Geology* 248, 119-139.

Ertel, W., O'Neill, H.S.-C., Sylvester, P.J., Dingwell, D.B., 1999. Solubilities of Pt and Rh in a haplobasaltic silicate melt at 1300 °C. *Geochimica et Cosmochimica Acta* 63, 2439-2449.

Ertel, W., Walter, M.J., Drake, M.J., Sylvester, P.J., 2006. Experimental study of platinum solubility in silicate melt to 14 GPa and 2273 K: implications for accretion and core formation in Earth. *Geochimica et Cosmochimica Acta* 70, 2591-2602.

Fortenfant, S.S., Dingwell, D.B., Ertel, W., Capmas, F., Birck, J.L., Dalpé, C., 2006. Oxygen fugacity dependence of Os solubility in haplobasaltic melt. *Geochimica et Cosmochimica Acta* 70, 742-756.

Fortenfant, S.S., Günther, D., Dingwell, D.B., Rubie, D.C., 2003. Temperature dependence of Pt and Rh solubilities in a haplobasaltic melt. *Geochimica et Cosmochimica Acta* 67, 123-131.

Franke, P., Neuschütz, D., 2005. The Landolt-Börnstein Database (<http://www.springermaterials.com>).

Giordano, D., Russell, J.K., Dingwell, D.B., 2008. Viscosity of magmatic liquids: a model. *Earth and Planetary Science Letters* 271, 123-134.

Grove, T.L., 1981. Use of PtFe alloys to eliminate the iron-loss problem in 1 atmosphere gas mixing experiments: theoretical and practical considerations. *Contributions to Mineralogy and Petrology* 78, 298-304.

Gudmundsson, G., Holloway, J.R., 1993. Activity-composition relationships in the system Fe-Pt at 1300 and 1400 °C and at 1 atm and 20 kbar. *American Mineralogist* 78, 178-186.

Hart, S.R., Zindler, A., 1986. In search of a bulk-Earth composition. *Chemical Geology* 57, 247-267.

Holzheid, A., Sylvester, P.J., O'Neill, H.S.-C., Rubie, D.C., Palme, H., 2000. Evidence for a late chondritic veneer in the Earth's mantle from high-pressure partitioning of palladium and platinum. *Nature* 406, 396-399.

Horan, M., Walker, R.J., Morgan, J., Grossman, J., Rubin, A., 2003. Highly siderophile elements in chondrites. *Chemical Geology* 196, 5-20.

Jakobsson, S., Oskarsson, N., 1994. The system C-O in equilibrium with graphite at high pressure and temperature: an experimental study. *Geochimica et Cosmochimica Acta* 58, 9-17.

Jansen, M., 2005. Effects of relativistic motion of electrons on the chemistry of gold and platinum. *Solid State Sciences* 7, 1464-1474.

Jochum, K.P., Nohl, U., Herwig, K., Lammel, E., Stoll, B., Hofmann, A.W., 2005. GeoReM: a new geochemical database for reference materials and isotopic standards. *Geostandards Geoanalytical Research* 29, 333-338.

Karpov, A., Konuma, M., Jansen, M., 2006. An experimental proof for negative oxidation states of platinum: ESCA-measurements on barium platinides. *Chemical Communications* 2006, 838-840.

Keller, N.S., 2008. Metals and volatiles in melts: an experimental and field study. Unpublished PhD thesis, Australian National University, Canberra, Australia.

Kessel, R., Beckett, J.R., Stolper, E.M., 2001. Thermodynamic properties of the Pt-Fe system. *American Mineralogist* 86, 1003-1014.

Kress, V.C., Carmichael, I.S.E., 1991. The compressibility of silicate liquids containing Fe₂O₃ and the effect of composition, temperature, oxygen fugacity and pressure on their redox states. *Contributions to Mineralogy and Petrology* 108, 82-92.

Laurenz, V., Fonseca, R.O.C., Ballhaus, C., Jochum, K.P., Heuser, A., Sylvester, P.J., 2013. The solubility of Pd and Ru in picritic melts: 2. The effect of sulfur. *Geochimica et Cosmochimica Acta* 108, 172-183.

Laurenz, V., Fonseca, R.O.C., Ballhaus, C., Sylvester, P.J., 2010. Solubility of palladium in picritic melts: 1. The effect of iron. *Geochimica et Cosmochimica Acta* 74, 2989-2998.

Lorand, J.-P., Luguét, A., Alard, O., 2008. Platinum-group elements: a new set of key tracers for the Earth's interior. *Elements* 4, 247-252.

Mann, U., Frost, D.J., Rubie, D.C., Becker, H., Audétat, A., 2012. Partitioning of Ru, Rh, Pd, Re, Ir and Pt between liquid metal and silicate at high pressures and high temperatures - implications for the origin of highly siderophile element concentrations in the Earth's mantle. *Geochimica et Cosmochimica Acta* 84, 593-613.

Marty, B., 2012. The origins and concentrations of water, carbon, nitrogen and noble gases on Earth. *Earth and Planetary Science Letters* 313-314, 56-66.

Médard, E., McCammon, C.A., Barr, J.A., Grove, T.L., 2008. Oxygen fugacity, temperature reproducibility, and H₂O content for nominally dry piston-cylinder experiments using graphite capsules. *American Mineralogist* 93, 1838-1844.

Médard, E., Schmidt, M.W., Schiano, P., 2004. Liquidus surfaces of ultracalcic primitive melts: formation conditions and sources. *Contributions to Mineralogy and Petrology* 148, 201-215.

O'Neill, H.S.-C., Dingwell, D.B., Borisov, A., Spettel, B., Palme, H., 1995. Experimental petrochemistry of some highly siderophile elements at high temperatures, and some implications for core formation and the mantle's early history. *Chemical Geology* 120, 255-273.

O'Neill, H.S.C., 1988. Systems Fe-O and Cu-O: Thermodynamic data for the equilibria Fe-"FeO", Fe-Fe₃O₄, "FeO"-Fe₃O₄, Fe₃O₄-Fe₂O₃, Cu-Cu₂O and Cu₂O-CuO from emf measurements. *American Mineralogist* 73, 470-486.

Palme, H., O'Neill, H.S.C., 2003. Cosmochemical estimates of mantle composition, in: Carlson, R.W. (Ed.), *Treatise on Geochemistry*. Elsevier-Pergamon, Oxford, pp. 1-38.

Righter, K., 2011. Prediction of metal-silicate partition coefficients for siderophile elements: an update and assessment of PT conditions for metal-silicate equilibrium during accretion of the Earth. *Earth and Planetary Science Letters* 304, 158-167.

Ringwood, A.E., 1977. Composition of core and implications for origin of Earth. *Geochemical Journal* 11, 111-135.

Rubie, D.C., Forst, D.J., Mann, U., Asahara, Y., Nimmo, F., Tsuno, K., Kegler, P., Holzheid, A., Palme, H., 2011. Heterogeneous accretion, composition and core-mantle differentiation of the Earth. *Earth and Planetary Science Letters* 301, 31-42.

Schmidt, M.W., Connolly, J.A.D., Günther, D., Bogaerts, M., 2006. Element partitioning: The role of melt structure and composition. *Science* 312, 1646-1650.

Schmidt, M.W., Gao, C., Golubkova, A., Rohrbach, A., Connolly, J.A.D., 2014. Natural moissanite (SiC) – a low temperature mineral formed from highly fractionated ultra-reducing COH-fluids. *Progress in Earth and Planetary Science* 1:27.

Simon, A.C., Pettke, T., Candela, P.A., Piccoli, P.M., Heinrich, C.A., 2007. The partitioning behavior of As and Au in S-free and S-bearing magmatic assemblages. *Geochimica et Cosmochimica Acta* 71, 1764-1782.

Stanley, B.D., Hirschmann, M.M., Withers, A.C., 2014. Solubility of C-O-H volatiles in graphite-saturated martian basalts. *Geochimica et Cosmochimica Acta* 129, 54-76.

Tsuzuki, A., Sago, S., Hirano, S.-I., Naka, S., 1984. High temperature and pressure preparation and properties of iron carbides Fe₇C₃ and Fe₃C. *Journal of materials science* 19, 2513-2518.

Wade, J., Wood, B.J., 2005. Core formation and the oxidation state of the Earth. *Earth and Planetary Science Letters* 236, 78-95.

Walker, D., Dasgupta, R., Li, J., Buono, A., 2013. Nonstoichiometry and growth of some Fe carbides. *Contributions to Mineralogy and Petrology* 166, 935-957.

Wang, Z., Becker, H., 2013. Ratios of S, Se and Te in the silicate Earth require a volatile-rich late veneer. *Nature* 499, 328–331.

Watson, E.B., 1987. Diffusion and solubility of Pt in C. *American Mineralogist* 72, 487-490.

Wetzel, D.T., Rutherford, M.J., Jacobsen, S.D., Hauri, E.H., Saal, A.E., 2013. Degassing of reduced carbon from planetary basalts. *Proceedings of the National Academy of Sciences of the United States of America* 110, 8010-8013.

Figure captions

Figure 1. (a) SEM backscattered electron images of typical run products, with a small bead of quenched liquid Pt-Fe-C alloy surrounded by silicate glass (B815 – 1.2 GPa – 1900 °C); (b) detailed view of quench textures in metallic alloy, showing dendritic growth associated with local variations in Pt (brightest), Fe and C (darkest) concentrations (B816 – 1.2 GPa – 1900 °C). Graphite blades (black) are interpreted as equilibrium graphite crystals and not considered during microprobe analysis of quenched alloys.

Figure 2. Variation of experimental oxygen fugacity as a function of the initially added Fe-Pt metal ($X_{\text{Fe}} = \text{Fe} / (\text{Fe} + \text{Pt})$ in weight). Experiments at ~1400 °C and ~1.2 GPa. The Fe-FeO (IW) reference buffer is from (Campbell et al., 2009), the CCO reference buffer from (Jakobsson and Oskarsson, 1994). The “real” iron-wüstite equilibrium using non-stoichiometric wüstite is also given for comparison (O'Neill, 1988), see note 1).

Figure 3. Time-resolved LA-ICP-MS analysis for two samples run at 1.5 GPa and 1360 °C with different starting materials: (a) experiment B1072 using the natural starting material is nanonugget-free, whereas (b) experiment B1087 run with oxidized and Pt-bearing starting material shows much higher concentration and broad “hills” indicative of nanonuggets.

Figure 4. (a) SEM backscattered electron image showing Fe-microspheres distribution in experiment B868 (1.2 GPa – 2100 °C); (b) time-resolved LA-ICP-MS analysis of sample B868, showing the absence of heterogeneity on the Pt signal; (c) SEM backscattered electron image showing heterogeneous nucleation of Fe-microspheres on the capsule wall.

Figure 5. Time-resolved LA-ICP-MS analyses for samples run at 1.2-1.5 GPa and 1360-1400 °C with oxidized and Pt-bearing starting material. All experiments have been analyzed under the same analytical conditions (25 Hz, 150-200 µm spot size), and the Pt counts is the sum of the counts on the three analyzed isotopes (^{194}Pt , ^{195}Pt , ^{196}Pt). The average number of counts for equilibrium experiments under similar conditions, using either natural (B1072 – 33 ppb Pt) or reduced (C1006 – 19 ppb Pt) starting material is given for comparison. The starting material for the oxidized starting material contains 3.2 ppm Pt. Concentrations in the static experiment (B1087) are highly heterogeneous and on average similar to concentrations in the starting material. Concentration in the central part of the dynamic experiment (Z300) are systematically lower than in the starting material and in the static experiment, but still significantly higher than the equilibrium values.

Figure 6. Metal / silicate partition coefficients (activity-based) as a function of absolute oxygen fugacity for three different experimental temperatures: 1360-1400 °C, 1600 °C and 1900 °C. For two points at 1375-1380 °C and one point at 1600 °C where Pt concentrations in glasses were below detection limit, we used the detection limit and added large error bars to indicate the range of possible values. The slope of the trends strongly suggests that Pt dissolves either as a neutral species or as a Pt^- anion under the experimentally investigated conditions, whereas it dissolves as Pt^{2+} under more oxidized conditions. Note that error bars for the activity coefficients are only estimated based on the analytical measurements. True errors including the uncertainties on the calculated activity coefficients are likely larger, but difficult to estimate. For experiments that did not use pure Pt (Bennett et al., 2014; Fortenfant et al., 2003), we used activity coefficients and oxygen fugacities as reported by the authors. For the experiments of Ertel et al. (2006), the oxygen fugacity was assumed to be on the CCO buffer (Jakobsson and Oskarsson, 1994). IW reference from Campbell et al. (2009).

Figure 7. Measured Pt concentrations in silicate melts at 1.2 GPa and 1900 °C as a function of oxygen fugacity. The excellent correlation between concentration and oxygen fugacity ($R^2 =$

0.957) is a strong indication of equilibrium achievement. Note also that the Pt concentration for the experiments with natural oxidized starting material and the reversal experiments with the reduced synthetic starting material plot on the same line.

Figure 8. Temperature dependence of Pt partition coefficients (activity-based) between metallic and silicate melts. For experiments that used pure Pt or Pt-Fe-C alloys, activity-coefficients were calculated using our ternary model. For other experiments (Bennett et al., 2014; Fortenfant et al., 2003; Mann et al., 2012), we used the activity reported by the authors. (a) Regression of our experimental data. The continuous line is a regression of all 21 data points, the dashed line a regression of the highest oxygen fugacity experiments, which fall into a restricted range of fO_2 ($-6.5 > \log fO_2 > -7.5$). (b) Comparison with previous data show that our experiments are consistent with the 0.5 -14 GPa nanonuggets filtered data of Ertel et al. (2006), the 2.0 GPa data of Bennett et al. (2014), and the 3.5-18 GPa data of Mann et al. (2012), but not with the 2.2-2.3 GPa microprobe data of Cottrell and Walker (2006). For the data of Ertel et al. (2006), only the highest duration experiments were kept at a given pressure and temperature to avoid artifacts linked to incomplete equilibration. The continuous line is the regression of our data from 8a, the dashed line a regression through Ertel et al. (2006) data. (c) The data of 8b have been sorted according to oxygen fugacity relative to the IW buffer. No clear oxygen fugacity trend is visible, but there is a tendency toward lower D at lower oxygen fugacity. All the experiments at $\log fO_2 < IW-2.0$ come from the same dataset (Cottrell and Walker, 2006).

Tables

Table 1. Starting materials

Sample	natural ^a	oxidized ^b	reduced ^b
SiO ₂	47.73	48.2(6)	45.2(5)
TiO ₂	0.59	0.61(7)	0.53(13)
Al ₂ O ₃	18.51	18.3(3)	16.9 (3)
FeO*	8.21	8.1(3)	13.7(2)
MgO	10.51	10.50(11)	10.2(4)
CaO	12.01	11.8(2)	11.7(4)
Na ₂ O	2.16	2.08(16)	2.0(3)
sum	99.72	98.70	99.12
Pt (ppb)	< 4	3200(700)	< 4

^aMajor element analysis from Donnelly-Nolan et al. (1991)

^bCompositions are microprobe analyses of glasses, renormalized to 100 %; the analytical total is given for information. Values in parentheses are either analytical errors or data dispersions, whichever is the largest, expressed as 2σ. The Pt concentrations have been obtained by LA-ICP-MS (see table 4 for analytical conditions).

Table 2. Static experiments

Run#	starting material (mg)				P (GPa)	T (°C)	b ^b hours	fO ₂
	silicate	Pt	Fe	Fe ₂ O ₃				(IW) ^a
<i>natural starting material</i>								
B1092	9.9	1.3	0.7		1.5	1360	48.2	0.6
B1072	9.9	0.7			1.5	1360	48.9	2.6
B665	20.2	0.8	10.3		1.0	1380	48.0	-0.9
B772	27.7	0.3	2.5		1.2	1600	20.7	-1.3
B771	29.0	0.7			1.2	1600	43.3	-0.9
B786	26.6	2.1		2.4	1.2	1600	25.8	1.0
B813	28.6	0.2	0.5		1.2	1700	10.1	-1.6
B775	28.2	0.2			1.2	1700	19.0	-0.5
B814	28.1	0.2			1.2	1800	3.2	-1.2
B864	25.2	0.4	9.2		1.2	1900	2.0	-1.9
B862	27.7	2.0	1.9		1.2	1900	2.0	-1.8
B816	26.2	1.8		2.3	1.2	1900	1.5	-1.3
B815	28.6	0.5			1.2	1900	1.5	-0.9
B863	26.7	1.2			1.2	2000	1.5	-1.6
B868	28.8	0.8	1.3		1.2	2100	0.5	-2.1
<i>oxidized starting material</i>								
B1087	9.9	0.8			1.5	1360	72.4	2.6
<i>reduced starting material</i>								
C1006	21.0	6.0			1.2	1400	48.1	2.4
B966	22.5	2.9	0.7		1.2	1600	24.1	-0.1
B967	23.5	1.4	1.0		1.2	1900	2.5	-1.8
B968	25.0	4.6			1.2	1900	2.0	-0.4

^aOxygen fugacity is given in log units relative to the IW buffer (Campbell et al., 2009).

^bRun duration in hours.

1051 *Table 3. Dynamic experiments*

Run#	starting material (mg)			static step			dynamic step					fO ₂
	silicate	Pt	Fe	P (GPa)	T (°C)	hours	P (GPa)	T (°C)	hours	°rpm	°g unit	(IW) ^b
<i>natural starting material</i>												
Z166	20.9	1.0	12.9	1.0	1400	70.5	0.7	1375	10.4	2017	1488	-0.7
Z164	30.0	3.0		1.5	1400	62.6	1.6	1380	11.1	2020	1492	2.4
Z186	27.1	2.2	^a 2.6	0.5	1600	25.4	0.7	1555	1.3	2014	1480	-0.1
Z184	29.1	1.2		1.2	1600	24.1	1.8	1560	2.1	2015	1481	1.1
Z205	27.5	4.6		1.2	1600	24.8	1.6	1615	1.0	2000	1459	0.9
Z204	25.5	0.7		1.2	1400	49.0	1.1	1655	2.0	2015	1481	1.0
<i>oxidized starting material</i>												
Z300	16.2	0.6		1.2	1400	68.8	1.0	1400	7.0	1300	1000	2.1

1052 ^aIn experiment Z186, iron has been added as Fe₂O₃

1053 ^bOxygen fugacity is given in log units relative to the IW buffer (Campbell et al., 2009).

1054 ^cAcceleration in turns per minute (rpm) and as a multiple of g (9.81 m.s⁻²).

1055

1056 *Table 4. Laser and ICP-MS conditions*

1057

1058 Laser parameter:

1059 Repetition rate: 25 Hz / 10 Hz; for low or “high” concentration

1060 Wavelength: 800 nm Pulse duration: < 150 fs

1061 Laser energy: 2 mJ Crater diameter: 120 - 200 μm

1062 Fluency: 6.4 - 17 J/cm²

1063

1064 ICP-MS (Perkin Elmer, Elan DRC II):

1065 Nebulizer gas flow: 0.85 L/min Ar Auxiliary gas flow: 0.85 L/min Ar

1066 Plasma gas flow: 17 L/min Ar Plasma power: 1400 W

1067 Carrier gas flow: 1 L/min He Auto lens on

1068 Isotopes: ²⁹Si, ⁴²Ca, ¹⁷⁸Hf, ¹⁹⁴Pt, ¹⁹⁵Pt and ¹⁹⁶Pt

1069 Dwell time: 10ms (Si, Ca, Hf), 50ms (Pt isotopes)

1070

1071

1072

1073

1074

1075

1076

1077

1078

1079

1080

1081

1082

1083 *Table 5. Experimental results (1360-1560 °C)*

Sample starting T (°C)	B1087 oxidized 1360	B1072 natural 1360	B1092 natural 1360	Z166 natural 1375	Z164 natural 1380	B665 natural 1380	C1006 reduced 1400	Z300 oxidized 1400	Z186 natural 1555
------------------------	---------------------	--------------------	--------------------	-------------------	-------------------	-------------------	--------------------	--------------------	-------------------

silicate (wt%)									
SiO ₂	48.4(4)	48.7(4)	46.9(8)	46.0(2)	49.9(2)	47.3(2)	45.9(7)	49.7(3)	46.0(3)
TiO ₂	0.65(6)	0.62(6)	0.55(8)	0.59(4)	0.62(2)	0.59(4)	0.53(6)	0.63(11)	0.57(2)
Al ₂ O ₃	18.9(2)	19.2(2)	18.2(2)	17.8(2)	19.0(2)	18.2(2)	18.0(3)	18.7(2)	18.1(3)
FeO*	7.0(2)	7.1(2)	11.9(4)	11.6(2)	4.62(9)	9.4(2)	9.1(2)	5.6(2)	11.79(8)
MgO	10.7(2)	10.2(2)	8.9(2)	10.20(9)	11.0(2)	10.4(2)	12.3(3)	10.8(2)	10.2(2)
CaO	11.7(4)	11.5(2)	10.9(4)	11.4(2)	12.3(2)	11.6(2)	12.0(2)	12.2(3)	11.3(2)
Na ₂ O	2.3(3)	2.42(13)	2.5(2)	2.22(5)	2.23(10)	2.24(11)	2.19(12)	2.1(2)	1.79(16)
sum	98.48	98.40	98.93	98.64	97.57	98.76	96.72	98.96	97.79
Pt (ppb)	nuggets	33(5)	6(2)	≤ 2	37(4)	≤ 2	19(3)	nuggets	39(9)
aFeO	0.0528	0.0539	0.0914	0.0893	0.0348	0.0720	0.0686	0.0426	0.0908
aPtO (10 ⁻⁷)		0.0923	0.0179	≤ 0.006	0.1028	≤ 0.006	0.0530		0.1106
alloy (wt%)									
	solid	solid	solid	liquid	solid	liquid	solid	solid	liquid
Fe	11.8(2)	11.8(2)	25.4(2)	69(2)	11.1(3)	88.2(16)	12.56(12)	12.2(2)	23.1(4)
Pt	88.2(4)	88.2(4)	74.6(4)	29(2)	88.9(5)	7.4(21)	87.4(4)	87.8(8)	76.9(12)
C	≤ 0.06	≤ 0.06	≤ 0.06	2.5(3)	≤ 0.06	4.4(4)	≤ 0.06	≤ 0.06	≤ 0.5
sum	100.7	101.8	102.4	102.4	98.6	101.3	99.8	99.8	98.4
X Fe	0.319	0.319	0.543	0.776	0.304	0.796	0.334	0.326	0.513
X Pt	0.681	0.681	0.457	0.093	0.696	0.019	0.666	0.674	0.487
X C	0	0	0	0.131	0	0.184	0	0	0
aFe	0.008	0.008	0.143	0.547	0.006	0.594	0.011	0.024	0.165
aPt	0.212	0.213	0.025	0.002	0.244	0.001	0.194	0.228	0.048
log fO₂	-7.62	-7.59	-9.63	-11.03	-7.57	-10.91	-7.46	-7.76	-8.56
delta CCO ^d	-0.16	-0.14	-2.18	-2.87	-0.34	-3.60	0.02	-0.28	-1.61
delta IW ^d	2.58	2.61	0.57	-0.72	2.40	-0.91	2.44	2.14	0.10
log D Pt		7.36	7.15	≥ 6.44	7.37	≥ 5.98	7.56		6.63

1084

1085

1086 *Table 5. Experimental results (continued, 1560-1700 °C)*

Sample	°Z184	B786	B966	B771	B772	Z205	Z204	B775	B813
starting	natural	natural	reduced	natural	natural	natural	natural	natural	natural
T (°C)	1560	1600	1600	1600	1600	1615	1655	1700	1700
Silicate (wt%)									
SiO ₂	41.5(8)	45.2(4)	46.5(4)	48.6(5)	47.7(3)	49.3(4)	49.7(3)	48.5(4)	48.3(4)
TiO ₂	0.16(14)	0.53(4)	0.56(14)	0.60(4)	0.58(4)	0.57(4)	0.60(6)	0.59(4)	0.59(4)
Al ₂ O ₃	17(2)	17.8(2)	17.5(3)	18.6(3)	18.40(14)	19.7(2)	18.9(3)	18.83(16)	18.68(14)
FeO*	2.0(6)	11.4(2)	10.7(3)	6.9(3)	8.6(2)	4.59(10)	5.06(14)	7.35(14)	7.07(14)
MgO	24(2)	12.2(2)	10.4(2)	10.9(2)	10.55(12)	10.9(2)	11.0(2)	10.8(3)	10.8(2)
CaO	3.2(9)	11.0(3)	12.0(5)	12.1(3)	11.9(4)	12.5(3)	12.3(2)	12.0(3)	12.1(3)
Na ₂ O	1.77(12)	1.81(8)	2.1(2)	2.19(14)	2.10(8)	2.24(12)	2.26(18)	1.70(10)	2.18(12)
sum	90.00	98.07	99.04	96.98	98.45	99.51	98.36	98.02	98.23
Pt (ppb)	173(6)	84(8)	113(15)	29(4)	≤ 6	182(20)	442(10)	191(6)	< 9
aFeO	0.0162	0.0867	0.0821	0.0525	0.0652	0.0346	0.0382	0.0560	0.0537
aPtO (10 ⁻⁷)	0.5015	0.2361	0.3189	0.0810	≤ 0.017	0.5054	1.2294	0.5362	≤ 0.025
alloy (wt%)									
Fe	11.4(4)	18.4(2)	23.8(2)	28.0(4)	85.7(16)	14.1(2)	13.5(2)	22.0(4)	73.5(9)
Pt	88.6(5)	81.6(8)	76.2(6)	72.0(7)	10 (2)	85.9(4)	86.5(4)	78.0(7)	23.4(11)
C ^b	≤ 0.06	≤ 0.06	≤ 0.06	≤ 0.5	4.3(6)	≤ 0.06	≤ 0.06	≤ 0.5	3.1(3)
sum	100.8	100.4	99.8	99.2	100.8	101.1	101.4	97.1	101.9
X Fe	0.310	0.427	0.521	0.576	0.790	0.364	0.355	0.496	0.778
X Pt	0.690	0.573	0.479	0.424	0.026	0.636	0.645	0.504	0.071
X C	0	0	0	0	0.184	0	0	0	0.151
aFe	0.010	0.103	0.141	0.283	0.604	0.025	0.024	0.184	0.599
aPt	0.258	0.126	0.045	0.031	0.002	0.178	0.195	0.076	0.007
log fO ₂	-7.19	-7.13	-8.01	-9.00	-9.47	-7.02	-6.79	-7.93	-8.99
delta CCO ^d	-1.29	-0.91	-1.79	-2.78	-3.25	-1.23	-0.80	-2.25	-3.31
delta IW ^d	1.09	1.02	0.14	-0.86	-1.33	0.90	0.96	-0.53	-1.59
log D Pt	6.71	6.65	6.15	6.58	≥ 6.12	6.55	6.20	6.15	≥ 6.43

1087

1088

1089 *Table 5. Experimental results (continued, 1800-2100 °C)*

Sample	B814	B968	B815	B816	B967	B862	B864	B863	B868
Starting	natural	reduced	natural	natural	reduced	natural	natural	natural	natural
T (°C)	1800	1900	1900	1900	1900	1900	1900	2000	2100
silicate (wt%)									
SiO ₂	48.0(3)	48.1(8)	47.7(3)	46.6(2)	45.6(4)	47.6(6)	48.6(4)	47.1(4)	43(2)
TiO ₂	0.58(4)	0.57(14)	0.57(4)	0.57(3)	0.48(9)	0.55(4)	0.60(6)	0.58(4)	0.51(4)
Al ₂ O ₃	18.7(3)	18.8(5)	19.3(2)	18.5(2)	19.0(4)	19.3(6)	18.5(3)	20.2(5)	26(2)
FeO*	7.6(2)	7.0(2)	7.47(10)	8.76(14)	10.6(3)	7.68(14)	6.98(14)	7.09(14)	7.2(2)
MgO	10.7(2)	10.9(2)	10.64(16)	11.29(14)	10.3(2)	10.6(2)	10.7(2)	10.7(2)	10.0(2)
CaO	12.0(3)	12.5(3)	11.9(3)	11.8(3)	11.8(3)	11.9(3)	12.1(3)	11.9(3)	11.0(4)
Na ₂ O	2.21(6)	2.14(14)	2.15(4)	2.19(12)	2.16(13)	2.15(12)	2.17(16)	2.11(14)	1.78(16)
sum ^a	98.89	99.38	98.40	98.37	99.41	99.63	99.94	99.16	99.16
Pt (ppb)	95(6)	735(37)	640(160)	342(30)	210(33)	195(21)	18(2)	504(18)	772(19)
aFeO	0.0576	0.0527	0.0567	0.0665	0.0814	0.0583	0.0530	0.0537	0.0543
aPtO (10 ⁻⁷)	0.2826	2.0529	1.7898	0.9566	0.5911	0.5457	0.0503	1.4068	2.1533
alloy (wt%)									
Fe	liquid	liquid	liquid	liquid	liquid	liquid	liquid	liquid	liquid
Pt	28.7(3)	16.0(4)	20.7(5)	29.2(5)	48.4(9)	55(2)	91.3(7)	27.9(5)	63.1(15)
C ^b	71.3(7)	84.0(8)	79.2(8)	70.8(7)	50.4(9)	43(2)	4.2(6)	70.3(8)	36(2)
C ^b	≤ 0.5	≤ 0.5	≤ 0.5	≤ 0.5	[1.2]	1.2(7)	4.5(5)	≤ 0.5	0.84(8)
sum ^a	98.8	99.8	99.3	99.7		101.1	101.6	98.6	100.9
X _{Fe}	0.584	0.400	0.477	0.590	0.710	0.754	0.804	0.581	0.816
X _{Pt}	0.416	0.600	0.523	0.410	0.212	0.169	0.011	0.419	0.133
X _C	0	0	0	0	0.078	0.077	0.185	0	0.051
a _{Fe}	0.368	0.117	0.218	0.414	0.566	0.634	0.658	0.432	0.770
a _{Pt}	0.049	0.201	0.124	0.060	0.028	0.021	0.003	0.078	0.026
log fO₂	-7.93	-6.49	-6.97	-7.39	-7.49	-7.87	-7.99	-7.14	-7.19
delta CCO ^d	-2.73	-1.73	-2.21	-2.63	-2.72	-3.11	-3.23	-2.77	-3.19
delta IW ^d	-1.21	-0.38	-0.85	-1.27	-1.37	-1.76	-1.87	-1.58	-2.14
log D Pt	6.27	5.99	5.84	5.80	5.67	5.58	5.77	5.74	5.09

1090 ^aSilicate melt and alloy compositions are renormalized to 100 %; the analytical total is given for
1091 information. Values in parentheses are either analytical errors or data dispersions, whichever is the
1092 largest, expressed as 2σ.
1093 ^bThe C concentration of solid alloys is below the detection limit of the microprobe (0.06 wt%). For Pt-
1094 rich liquid alloys, C cannot be analyzed accurately due to its low concentration (< 0.5 wt%). Values
1095 between brackets are estimated from the sums of analyses not including C.
1096 ^cExperiment Z184 is contaminated through interactions with the piston-cylinder assembly. The low
1097 total likely indicates presence of boron, originating from the surrounding Pyrex glass.
1098 ^dOxygen fugacity is given in log units, as absolute value, and relative to the CCO (Jakobsson and
1099 Oskarsson, 1994) and IW (Campbell et al., 2009) buffers.
1100

